Journal of Magnetic Resonance **152,** 247–258 (2001)
doi:10.1006/jmre.2001.2408, available online at http://www.idealibrary.com on IDEAL®

High Spatial Resolution Multi-Site EPR Oximetry

The Use of a Convolution-Based Fitting Method

Oleg Y. Grinberg,*,[1] Alex I. Smirnov,† and Harold M. Swartz*

*EPR Center for the Study of Viable Systems, Department of Radiology, Dartmouth Medical School, Hinman Box 7785, Vail Building, Room 703, Hanover, New Hampshire 03755; and †Department of Chemistry, North Carolina State University, Campus Box 8204, Raleigh, North Carolina 27695-8204

Received March 2, 2001; revised July 10, 2001; published online September 4, 2001

We describe a new method to enhance the spatial resolution of multi-site electron paramagnetic resonance (EPR) oximetry. The method is suitable for any shape (density distribution function) of a solid paramagnetic material implanted in tissue. It corrects distortions of lineshapes caused by the gradient and thus overcomes limitations of previous multi-site EPR oximetry methods that restricted the ratio of the particle size to the distance between sites. The new method is based on consecutive applications of magnetic field gradients with the same direction but with a different magnitude and uses a convolution-based fitting algorithm to derive Lorentzian EPR linewidths of each individual peak of the EPR spectrum. The method is applicable for any particulate EPR oxygen sensitive materials whose EPR spectra can be approximated by a Lorentzian function or a superposition of Lorentzian functions. By incorporating this model of the lineshape in the data processing, we are able to decrease significantly the number of parameters needed for the calculations and to recover the oxygen concentration, even from quite noisy spectra. We (i) describe our method and the data-processing algorithm, (ii) demonstrate our approach in model and *in vivo* experiments, and (iii) discuss the limitations.

Key Words: **EPR oximetry; multi-site EPR oximetry; tissue pO_2; convolution-based fitting.**

INTRODUCTION

The local oxygen concentration is an important parameter for many physiological and pathophysiological processes. Understanding of these processes calls for accurate and minimally invasive measurements of local oxygen. Up to now most direct measurements of tissue pO_2 have been carried out using oxygen electrodes. Although accurate, these measurements suffer from some limitations due to trauma associated with positioning of the electron in the tissue and the difficulty of making repetitive measurements in the same animal at exactly the same place. Electron paramagnetic resonance (EPR) oximetry appears to be a new method capable of overcoming these problems. Particularly, the use of particulate oxygen probes makes EPR oximetry very suitable for repetitive measurements of pO_2 at specific sites in biological samples both *in vitro* and *in vivo* (*1–8*).

The EPR oximetry method is based on observing effects of molecular oxygen on EPR spectra in either continuous wave (CW) or time-domain experiments. Several different types of oxygen-sensitive paramagnetic materials have been developed for this use, including both soluble and particulate materials (for example, nitroxide radicals, coals such as fusinite, carbohydrate chars, and metalloorganic compounds such as lithium phthalocyanine, LiPc). For nitroxide radicals and most particulate probes, the main mechanism of the effect of oxygen on the EPR spectra is the shortening of both spin–spin and spin–lattice relaxation times by Heisenberg exchange during bimolecular collisions, although for several particulate probes dynamic dipolar interaction with oxygen could also affect a relaxation rate.

Repetitive oxygen measurements with EPR require that the probes remain in place for the entire period of the experiments and that their properties are unaffected by local metabolic processes and local changes in the environment such as variations in pH. Several oxygen probes including LiPc, coals, and some carbohydrate chars do satisfy all these requirements (*2, 4, 6, 7*). LiPc is a particularly attractive probe for EPR oximetry because its CW EPR spectrum is very narrow (with a peak-to-peak ~30-mG linewidth in the absence of oxygen), the spectrum is modeled well by a Lorentzian function, and the response to oxygen is a linear function of pO_2 (*3*). In recent years EPR oximetry with LiPc has been applied to study the effects of various anesthetics on brain oxygenation (*5, 9–11*) and the effects of a hemoglobin shifter on cerebral pO_2 under baseline conditions and after acute hemorrhage (*12, 13*). Recently this technique was utilized in the study of acute cerebral ischemia and reperfusion, induced by selective reversible unilateral occlusion of the middle cerebral artery of the rat brain. Acute changes of the pO_2 in both the ischemic and control side of the brain were measured simultaneously over the entire experimental period (*14*). The latter study employed magnetic field gradients to simultaneously monitor pO_2 at several sites.

[1] To whom correspondence should be addressed. Fax: (603)650-1717. E-mail: oleg.grinberg@dartmouth.edu.

1090-7807/01 $35.00

Experimental conditions for multi-site EPR oximetry and initial *in vivo* demonstrations were previously described in (*15*). Particularly, if the size of the implanted probe particles is sufficiently small compared with the distances between the implants, then the magnitude of a magnetic field gradient could be chosen so the individual EPR spectra from the implants become resolved and not distorted to any significant extent by the magnetic field gradient. It was estimated that for implanted particles with rectangular shapes and length, about 0.2 mm optimally resolved spectra with minimal (<1%) distortion of Lorentzian shapes are obtained if the distance between the implants exceeds 1.8 mm. It also was estimated that in order to keep the distortion minimal (e.g., less than 1%), the maximum magnitude of the gradient should be limited. For LiPc particles that are 0.2 mm long and have peak-to-peak EPR linewidths of 30 mG, the gradient should not be greater than 0.34 G/cm to avoid distortions in excess of 1%.

Although (*15*) was a valuable demonstration that EPR oximetry can provide pO_2 measurement in several sites simultaneously, the technique employed in that study has several limitations. First, the method imposes special geometrical requirements on implanted particles (particularly size to inter-site ratio). Secondly, the requirement of not disturbing the lineshape of individual implants limits the maximum magnitude of the magnetic field gradient that could be applied, and this limits the spectral resolution. In other words, the method lacks corrections of the measured EPR linewidth for distortions caused by magnetic gradients of arbitrary magnitudes and arbitrary shape/density functions of a solid paramagnetic material implanted in the tissue, and therefore it is not applicable if the local oxygen concentration varies over the length of the implant (site) or if the sites are close to each other.

To overcome the current limitations of multi-site EPR oximetry and to improve its spatial resolution, we have developed a new method that is based on consecutive applications of magnetic field gradients with the same direction but different magnitudes. The method is suitable for any shape (density distribution function) of a solid paramagnetic material implanted in the tissue because it allows us to correct for lineshape distortions caused by the gradient, and thus to overcome the previous limitation on the particle size, inter-site distance ratio.

The use of magnetic field gradients with two different magnitudes has been described previously to reconstruct one-dimensional density functions for two paramagnetic centers having overlapping but different and known EPR spectra in the absence of a gradient (*16*). The method is based on solving a system of equations in the frequency domain with a consequent optimized filtering of the inverse Fourier transform (*16*). The method we present here is different. Instead of recovering unknown density distribution function(s), our goal is to get an accurate measure of undistorted lineshapes. By incorporating a model of the lineshape in the data processing, we were able to decrease significantly the number of parameters that were needed and to recover the oxygen concentration even from quite noisy spectra. Below we (i) describe our method and the data-processing algorithm, (ii) demonstrate our approach in model and in vivo experiments, and (iii) discuss the limitations.

RESULTS

Theoretical Considerations

Application of inhomogeneous magnetic fields allows one to encode the spatial information in the EPR spectra. Generally, EPR spectrum $J(B)$ is given by an integral

$$J(B) = \int_V f(B - B_0(\boldsymbol{r}))\mu(\boldsymbol{r})\, d\boldsymbol{r}, \qquad [1]$$

where $\mu(\boldsymbol{r})$ is the distribution (density) function of paramagnetic centers and $f(B(\boldsymbol{r}))$ is the lineshape function. When the external magnetic field is changing linearly, i.e., $B(r) = B_0 + r(\partial B/\partial r) = B_0 + r\ gradB$, Eq. [1] is simplified to a convolution integral (*17*) which can be written in either spectral [2] or spatial [3] coordinates:

$$\begin{aligned} J(B, gradB) &= \int_{-\infty}^{\infty} p(B')\, f\left(B - B', \Delta B_{1/2}\right) dB' \\ &= p(B) * f(B) \qquad [2] \\ J(r, gradB) &= \int_V p(r')\, f\left(r - r', \Delta r_{1/2}\right) dr' \\ &= p(r) * f(r). \qquad [3] \end{aligned}$$

In these equations p is the projection of the density of paramagnetic centers on the direction of the gradient, f is the lineshape of EPR spectrum in the absence of the gradient, and $*$ denotes the convolution.

For the purpose of this paper it is convenient to use spatial coordinates (i.e., Eq. [3]). It is worth noting that in this scale the projection function $p(r)$ is independent of the magnitude of the magnetic field gradient $gradB$, but the lineshape function $f(r, \Delta r_{p-p})$ changes with the magnitude of the magnetic field gradient because $(r - r_0) = (B - B_0)/gradB$.

The EPR lineshape for many oxygen-sensitive materials can be approximated well by a Lorentzian function (e.g., for LiPc)

$$f(B) = \frac{2A}{\pi} \frac{\Delta B_{1/2}^2}{\Delta B_{1/2}^2 + 4(B_0 - B)^2} \qquad [4]$$

or as a superposition of a few Lorentzian functions (e.g., carbohydrate chars). In Eq. [4] $\Delta B_{1/2}$ is the linewidth at half of the line height and A is the value of the double integral that is proportional to the number of spins. When transformed from spectral coordinate scale B to the spatial coordinates r, the width of the

lineshape function scales with the gradient:

$$\Delta r_{1/2} = \frac{\Delta B_{1/2}}{gradB}. \quad [5]$$

We record two EPR spectra $J_i(r, (gradB)_i); i = 1, 2$ at two different magnetic field gradients $(gradB)_2 > (gradB)_1$ applied in the same direction. Thus

$$\begin{aligned} J_1(r, (gradB)_1) &= p(r) * f\left(r, \left(\Delta r_{1/2}\right)_1\right) \\ &= p(r) * \left[f\left(r, \left(\Delta r_{1/2}\right)_2\right) * f\left(r, \Delta r_{1/2}\right)\right] \\ &= J_2(r, (gradB)_2) * f\left(r, \Delta r_{1/2}\right), \end{aligned} \quad [6]$$

where

$$\Delta r_{1/2} = \left(\Delta r_{1/2}\right)_1 - \left(\Delta r_{1/2}\right)_2 = \Delta B_{1/2}\left[\frac{1}{(gradB)_1} - \frac{1}{(gradB)_2}\right]. \quad [7]$$

Equation [6] could be derived because the convolution of two Lorentzian functions gives a Lorentzian function with a width equal to the sum of the initial widths. Equation [6] shows that when expressed in spatial coordinates, the EPR spectrum $J_1(r)$ taken at a smaller gradient can be presented as a convolution of a spectrum $J_2(r)$ taken with a larger gradient $(gradB)_2$ and a Lorentzian function $f(r, \Delta r_{1/2})$ with a linewidth $\Delta r_{1/2}$ that depends on the undistorted linewidth $\Delta B_{1/2}$ and the magnitudes of the two gradients as given by Eq. [7]. When the second gradient is much larger than the ratio of the EPR linewidth to the size of the solid probe that gives rise to the EPR signal, the projection function $p(r)$ is well approximated by $J_2(r)$ and Eq. [6] reduces to Eq. [3]. This means that if the projection function $p(r)$ is known from another experiment, then Eq. [2] or Eq. [3] could be applied to derive the width of the EPR spectrum and no correction by Eq. [7] is necessary. However, in a typical *in vivo* EPR oximetry experiment, the projection function $p(r)$ cannot be determined separately (e.g., the shape of the LiPc crystal is irregular and its orientation after implantation is unknown or there is an uncertainty whether the crystal has broken apart during the implantation). Because the signal-to-noise ratio limits the maximum gradient, the more general Eqs. [6] and [7] can be used instead. In the latter case a convolution integral is constructed from the experimental spectrum $J_2(r)$ rescaled according to spatial coordinate $r = B/(gradB)_2$ and a Lorentzian function $f(r, \Delta r_{1/2})$ which is generated digitally. This convolution integral is then fitted to another experimental spectrum $J_1(r)$ measured with a smaller gradient $(gradB)_1$. The same kind a convolution-based fitting was previously described to simulate broadening of isotropic and anisotropic EPR spectra or selected parts of the spectra by additional isotropic interactions (*18, 19*). It has been shown that the linewidth, double-integrated intensity, and position of the "broadening" function f in a convolution integral given by Eq. [2] or Eq. [3] can be derived using Levenberg–Marquardt optimization.

Summary of the Method

The method of high spatial resolution, multi-site EPR oximetry is organized as follows:

1. A magnetic field gradient is applied to separate the EPR signals from different implants of oxygen sensitive solid material (such as LiPc) injected into a tissue of interest. Initially, the direction of the gradient can be varied to optimize the spectral resolution at a particular gradient strength. The key assumption is that only a limited number of particles of the probe material are present, so they can be resolved by applying magnetic field gradient. (In a typical *in vivo* experiment, particulate oxygen probes are injected through a needle so they are principally distributed along the direction of the injection, and thus could be resolved with one-dimensional magnetic field gradients.)

2. Once the direction of magnetic field gradient is optimized, two spectra $J_1(r, (gradB)_1)$ and $J_2(r, (gradB)_2)$ are taken at two different magnitudes of the gradient $(gradB)_2 > (gradB)_1$ of the same direction. If spectrum J_1 was recorded over the spectral window $\Delta B_1 = B_{initial} - B_{final}$ (scan range of the magnetic field), then in order to keep the same spatial coordinate scale, a second spectrum at a larger gradient $(gradB)_2$ has to be rescaled. For this reason the second spectrum should be taken over a larger window $\Delta B_2 = \Delta B_1 \times (gradB)_2/(gradB)_1$ and digitized with the same number of data points as the first spectrum. Some spectrometers may not allow setting desirable spectral windows ΔB_1 and ΔB_2. Then the taken spectra should be rescaled/interpolated to desirable windows with computer software such as EWVoigt or others.

3. The next step is the least-squares fitting according to the convolution equation [6]. During the fitting the experimentally measured spectrum J_2 taken at a larger magnetic field gradient serves as a fixed function, which we call "envelope." This spectrum is digitally convolved with a Lorentzian broadening function f that is computer-generated. The result of the convolution is compared with J_1, and the parameters of the Lorentzian broadening function (linewidth, amplitude, position, and, if desired, the contribution of any out-of-phase dispersive component) are optimized. This fitting can be done effectively and accurately using a fast convolution algorithm combined with Levenberg–Marquardt optimization, which we described previously (*18, 19*) and which is utilized in the EWVoigt program. The algorithm allows an arbitrary fixed inhomogeneous envelope function to be included directly in the fitting procedure. The fitting is carried out by comparing two spectra taken at magnetic field gradients of different magnitudes. This leads to a one-linewidth parameter fitting, and thus increases the accuracy of computation. The algorithm also provides estimates of the uncertainties of parameters from a standard covariance matrix procedure (*18, 19*).

4. During the fitting it is more convenient to use the magnetic field scale corresponding to the spectrum J_1. Then the

"best fit value" for the width of the Lorentzian broadening function derived from the fit $\Delta B_{1/2;FIT}$ is related to the "natural" (or undistorted) linewidth $\Delta B_{1/2}$ of an oxygen probe by a modified Eq. [7]

$$\Delta B_{1/2;FIT} = \Delta r_{1/2}(gradB)_1 = \Delta B_{1/2}[1 - (gradB)_1/(gradB)_2]. \quad [8]$$

Results with Model Spectra

The algorithm was tested on a set of computer-simulated spectra. Figure 1 depicts one of the models used for such a test. In this model we assume that the oxygen-sensitive EPR material is uniformly distributed within a cylinder and a parallelepiped with the same spin density. The cross sections of these shapes are shown in Fig. 1A. Figure 1B shows the simplest projection of the density of paramagnetic centers onto a direction of the magnetic field gradient. The diameter of the cylinder was set to be equal to the length of the parallelepiped edge in the direction of the gradient and equal to the spacing between the two shapes, Δr. It was assumed that in a uniform magnetic field, the shape of the EPR spectra from each of the objects is a Lorentzian; however, the linewidth corresponding to the parallelepiped is 80% of that for the cylinder (i.e., $0.8 \times \Delta B_{1/2}$ and $\Delta B_{1/2}$, respectively). These two EPR spectra, whose signal intensity (double integral) is proportional to the number of spins in each of the two objects (for uniform samples it is proportional to their volumes), are superimposed in Fig. 1C and correspond to $gradB = 0$. When the magnetic field gradient was set to $\Delta B_{1/2}/\Delta r$, the EPR spectra from each of the objects became resolved. We have simulated a series of EPR spectra from such a sample at different values of magnetic field gradients (Figs. 1D–1H). To better visualize the lineshapes, all spectra in this figure were normalized by peak-to-peak amplitude. The magnitudes of the magnetic field gradient for the rest of the spectra, measured in units of $\Delta B_{1/2}/\Delta r$, were as follows: D, 0.5; E, 1.0; F, 2.0; G, 4.0; and H, 8.0. Spectra in Figs. 1D through 1H are shown in a scale of the spatial coordinate r. This set of spectra illustrates that for spectra converted to the spatial coordinate r, an increase in the gradient results in an apparent linewidth narrowing. Thus, the relative contribution of natural lineshape to the recorded spectra progressively decreases from ca. 66% in Fig. 1C to only 11% in Fig. 1H.

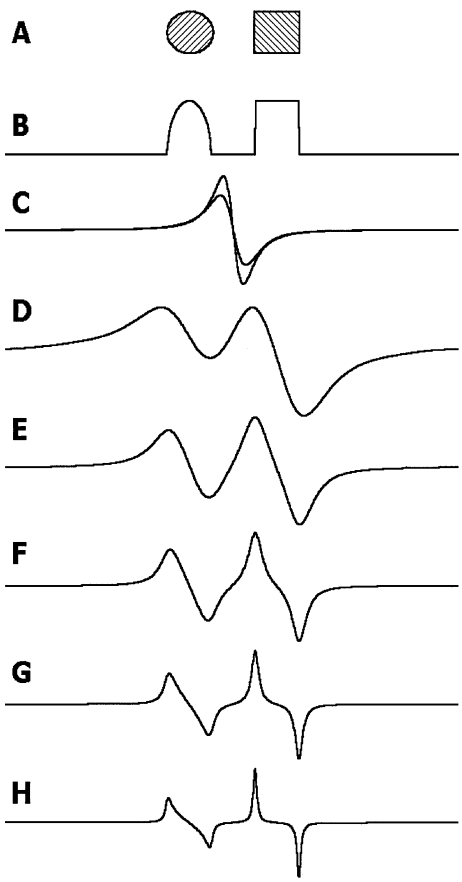

FIG. 1. The shapes of phantoms, distributions of paramagnetic centers, and computer-simulated EPR spectra in a model system: A, cross sections of a cylinder and a parallelepiped containing an oxygen-sensitive EPR material of uniform density; B, a projection of the density of paramagnetic centers onto the direction of the magnetic field gradient; C, computer-simulated "noise-free" EPR spectra without magnetic field gradient; D, E, F, G, and H, simulated spectra with magnetic field gradient shown in the spatial coordinate r; the magnitude of the gradient is $gradB = 0.5, 1, 2.0, 4.0,$ and 8.0, respectively, measured in units of $\Delta B_{1/2}/\Delta r$. See text for additional details.

Because the widths of Lorentzian functions corresponding to each of the shapes are different, Eq. [6] cannot be applied to simulate the entire spectrum taken with a magnetic field gradient, but the parts of the spectra could be simulated instead. Clearly, when the magnetic field gradient $gradB \gg \Delta B_{1/2}/\Delta r$, where Δr is the distance between two objects, there is no overlap in the spectra and so they can be simulated separately (for example, by splitting the spectrum into two halves or by optimizing the simulation results for only a part of the spectrum). However, for technical reasons such large gradients could be unattainable. Thus, in practice, the spectra could have some partial and even substantial overlap such as in Figs. 1D and 1F. Even in the latter case our method should be applicable depending on the magnitude of linewidth gradient (i.e., the difference in the linewidth) present in the system.

To demonstrate this, let us consider the fitting of the partially resolved spectrum shown in Fig. 1E. In these fittings the spectrum from Fig. 1G was taken as a nonadjustable envelope function (i.e., function J_2 in Eq. [6]) and fitted to spectrum Fig. 1E (i.e., function J_1 in Eq. [6]) using the convolution Eq. [6]. Results of typical fittings are shown in Fig. 2. Initially, the lower field part of the spectrum (left from the dashed line in Figs. 2A and 2B) was chosen as the interval to be fit. The best-fit result is superimposed on the spectrum (Fig. 2A) and the residual (the difference between the spectrum and the fit) is shown at the

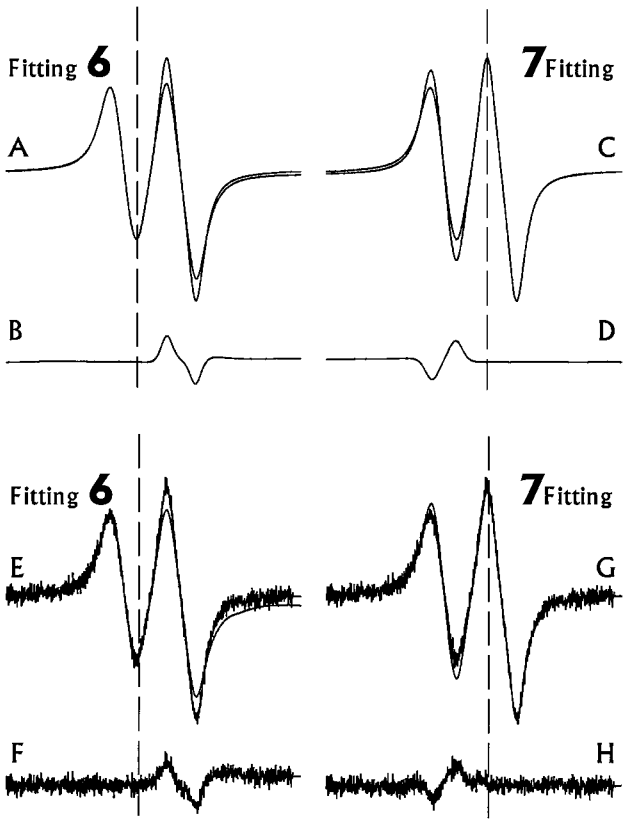

FIG. 2. Results of least-squares fitting of the computer-simulated "noise-free" spectrum in Fig. 1E using the spectrum in Fig. 1G as a nonadjustable "envelope" function in the convolution Eq. [6]: A, the lower field part of the spectrum was chosen as the interval to be fit and C, the high field part of the spectrum was chosen as the interval to be fit. The simulated spectra are shown as dotted lines. Figures 2B and 2D are the residuals (the difference between the spectra and the fits). Spectra in Figs. 2E and 2G illustrate least-squares fitting of the same spectra as in upper portion of the figure but adding a computer-generated Gaussian noise. The standard deviation of the noise was chosen to be 2% of the signal peak-to-peak amplitude.

bottom (Fig. 2B). While the residual is essentially a straight line over the interval that was fit, the deviation between the spectrum and the simulation outside the interval is rather large. This deviation is due to the difference in linewidths corresponding the two sites. We then can estimate the shape of the residual assuming that the simulations for one of the sites are "perfect." The spectra J_1 and J_2 we used in the fitting are actually superpositions of the spectra from the individual sites which we denote with $^{(a)}$ and $^{(b)}$

$$J_i = J_i^{(a)} + J_i^{(b)}, \quad i = 1, 2.$$

Equation [6] is still valid but only for the individual spectra: $J_1^{(a)} = J_2^{(a)} * f^{(a)}$, $J_1^{(b)} = J_2^{(b)} * f^{(b)}$, where $f^{(j)}$ are the Lorentzian functions of different widths. If the fit for the site (a) is "perfect" (i.e., the broadening function for the spectrum J_2 is given by $f^{(a)}$), then the fit residual R can be estimated as follows:

$$\begin{aligned} R &= J_1(r, (gradB)_1) - J_2(r, (gradB)_2) * f\left(r, \Delta r_{1/2}^{(a)}\right) \\ &= \left(J_1^{(a)} + J_2^{(b)}\right) - \left(J_2^{(a)} * f^{(a)} + J_2^{(b)} * f^{(a)}\right) \\ &= J_1^{(b)} - J_2^{(b)} * f^{(a)} = J_2^{(b)} * \left(f^{(b)} - f^{(a)}\right) \\ &\approx J_2^{(b)} * \left[\frac{\partial f\left[r, \left(\Delta r_{1/2}^{(a)} + \Delta r_{1/2}^{(b)}\right)/2\right]}{\partial \Delta r_{1/2}}\left(\Delta r_{1/2}^{(b)} - \Delta r_{1/2}^{(a)}\right)\right]. \end{aligned} \quad [9]$$

The estimate given by [9] shows that when the difference in linewidths between the "broadening" functions $f^{(b)}$ and $f^{(a)}$ is small, then the residual R is given by a convolution of the spectrum $J_2^{(b)}$ taken at a larger gradient with a partial derivative of the broadening function with respect to the linewidth. The amplitude of the residual is proportional to the linewidth difference ($\Delta r_{1/2}^{(b)} - \Delta r_{1/2}^{(a)}$). Thus, as one could expect, a decrease in the linewidth difference decreases the magnitude of the residual. Because the partial derivative of the Lorentzian function with respect to the linewidth decays more rapidly than the Lorentzian function, the residual from the fit rapidly approaches zero and its effect on the fitting within the interval is expected to be small (Fig. 2).

Effects of Noise and the Interval to Be Fit

There are two major potential sources of errors in our method: random noise in the experimental data and spectral overlap.

The uncertainties caused by random noise can be evaluated using the standard covariance matrix method. Previously it has been shown that this method provides correct estimates of linewidth errors in EPR experiments (*20*). The errors due to random noise decrease with increased EPR signal-to-noise ratios. It is worthwhile to note here that the covariance matrix method provides correct estimates under two conditions: the noise has a distribution that is Gaussian or close to that and the spectral model is adequate for the experiment.

The magnitude of errors caused by a partial overlap depends on the size and distance between adjacent sites, and hence no a priori generalizations can be made. The errors with our fitting model would contribute significantly only at a small field gradient. Increasing the applied field gradient can decrease spectral overlap and therefore errors caused by this overlap. However, a partial spectral overlap is likely to be encountered frequently because in many cases the EPR signal-to-noise ratios limit the maximum magnitude of the magnetic field gradient that can be employed. Therefore one can expect that for each particular experiment a range of optimal gradient values could be defined at which the errors due to noise will exceed the uncertainty due to spectral overlap.

To illustrate this point, let us consider the partially resolved simulated spectra shown in Figs. 1E and 1G. This extent of partial resolution is quite typical for EPR experiments *in vivo*. To simulate the effect of random noise on the fitting procedure

and error estimates, we have added a Gaussian noise to the noise-free model spectra shown in Figs. 1E and 1Q. It was previously shown that the noise in EPR follows the Gaussian distribution quite well (*21*). The standard deviation of the Gaussian noise was chosen to be 2% of the signal peak-to-peak amplitude for each of the spectra. The model "noisy" spectrum is overlapped with the results of least-squares simulations for each of the intervals. The results of the fits are shown in Figs. 2E and 2G. Residuals are shown in Figs. 2F and 2H. The results of digital convolution look less "noisy" in Figs. 2E and 2G because the convolution with computer-generated Lorentzian functions during the fitting procedure effectively filters high frequency noise. Even at this relatively high noise level, the extracted linewidths were quite similar to those we used in our modeling

$$\left(\Delta B_{1/2}\right)_{fit,a} / \Delta B_{1/2} = 1.005 \pm 0.036$$

(vs. 1.000 for the cylinder in the model) and

$$\left(\Delta B_{1/2}\right)_{fit,b} / \Delta B_{1/2} = 0.765 \pm 0.020$$

(vs 0.800 for the parallelepiped in the model). Note that the estimated errors, which correspond to the 68% confidence intervals, are in line with the deviation we observed. This illustrates that in the presence of noise with a standard deviation similar to or larger than that shown in Fig. 2 (this noise level is typical for *in vivo* experiments) and similar sample geometries, the errors in the extracted parameters are primarily determined by the random noise, not by the unaccounted for contributions from other nearby sites. Note that no digital filtering was applied to the spectra shown in Figs. 2E and 2F: all the linewidths were measured by the least-squares fitting procedure we described.

We also have estimated the effect of a nonzero residual from the second site on the results of least-squares simulations within the interval to be fit. The contribution of the residual depends on the choice of the interval that is fit and the magnitudes of the gradients applied for the spectra J_1 and J_2. For these estimates we used the series of noise-free simulated spectra shown in Fig. 1. When no noise is present, the errors in linewidth are caused by the imperfections of the model (i.e., how rapidly the residual R, Eq. [9], approaches zero within the interval to be fit). Contributions of other factors, such as "wrap-around" effects discussed in (*19*), are negligible for the spectra shown in Fig. 2. Note that the error we discuss here is not an estimate from the covariance matrix method but the deviation between the linewidths derived from the fit and the exact linewidth we put in the model.

The deviation of the extracted linewidth as a function of the interval to be fit was investigated. The simulations were carried out for the same partially resolved spectral pair as in Fig. 2A, but the right border of the interval was varied. The modulus of the deviation of the extracted linewidth (in percentages) for the left site is plotted in Fig. 3, filled circles, as a function of the extent of the interval in percent of the overall spectral width. The left border of the interval was fixed at the beginning of the spectrum. Thus, the 50% point in the graph corresponds to the interval covering the left 50% of the spectra in Fig. 2A. The slope and the offset of the baseline, and all the parameters of the Lorentzian broadening function, were allowed to vary during the optimization, with the exception of the dispersive contribution, which was set to zero.

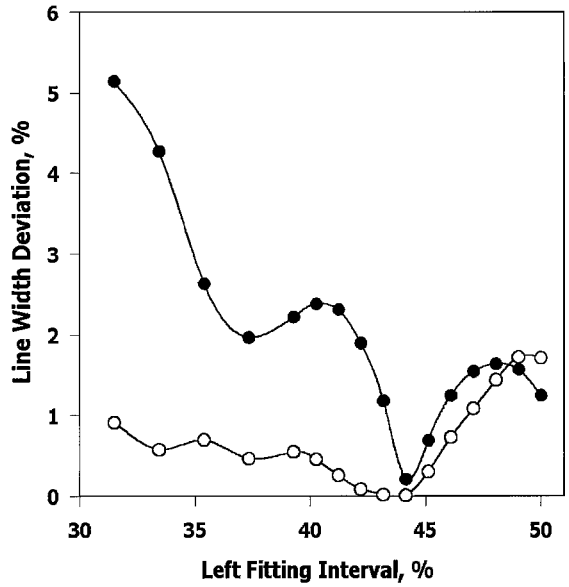

FIG. 3. The computed deviations of the extracted linewidth (in percent) as a function of the extent of the interval that was fit (in percent of the overall spectral width) for the pairs of the simulated spectra shown in Fig. 1: filled circles correspond to the spectral pair in Figs. 1E and 1G and open circles correspond to those shown in Figs. 1F and 1H. The left border of the interval was kept fixed at the beginning of the spectrum and the right border of the interval was varied.

Although the shape of the curve in Fig. 3 is rather complex, several observations can be made. First, the minimum error occurs for the interval to be fit at around 44%. The right border of such interval is shown in Fig. 2A by a dashed line. Secondly, over a large extent of the intervals (e.g., from 37 to 50%) the maximum error, even for these overlapping spectra, is less than 2.3%, which is quite acceptable for many practical applications. When the interval to be fit is less than 36% (36% corresponds to the first maximum of the spectrum shown in Fig. 2A), the linewidth error increases because for these fitting intervals there are rather large uncertainties in the position of the spectrum and the baseline coefficients. In the presence of noise the fitting of only the left "wing" of the spectrum also is impractical because the intensity is low.

When the magnitudes of the magnetic field gradients for both the J_1 and J_2 spectra were doubled (spectra in Figs. 1F and 1H), the linewidth deviation as a function of the extent of the interval changed (Fig. 3, open circles). The maximum error decreased significantly except for the intervals approaching 50%. However,

the position of the minimum error remained approximately the same (43–44% intervals). Thus, for the optimal results the intervals to be fit should be chosen close to those shown in Fig. 2.

We also have estimated the magnitudes of these errors for all possible pairs of spectra shown in Fig. 1 when the fitting interval is close to the optimal (i.e., as depicted in Fig. 2). From these simulations, the largest deviation between the actual and extracted parameters was found to be about 2.6% for the spectral pair with the lowest resolution (spectra in Figs. 1D and 1F). When the gradient was set to be equal to $\Delta B_{1/2}/\Delta r$, this deviation dropped to 1.2%. Typically, this level of error is quite acceptable for practical measurements. For the best resolved pair (spectra in Figs. 1G and 1H), this deviation was less than 0.2%.

Results with a Phantom Sample

The method was further tested using a phantom made out of LiPc crystals sealed in two separate glass capillaries (i.d. = 0.8 mm, about 1 mg of LiPc in each capillary). The capillaries were filled with oxygen–nitrogen gas mixtures containing about 1 and 2% of oxygen, respectively (corresponding peak-to-peak EPR linewidths were 56 ± 1 and 68 ± 1 mG). The capillaries were placed inside an "external-loop" EPR resonator so the distance between the axles of the capillaries was approximately 1.4 mm, and the vector between LiPc crystals was aligned along the external magnetic field. The magnetic field gradient was aligned in the same direction. Figure 4 shows a series of EPR spectra from the phantom as a function of the magnetic field gradient. This series demonstrates that when the distance between the capillaries is comparable with their diameter, the spectral lines corresponding to the individual capillary become resolved only with relatively large gradients (Figs. 4C and 4D) that clearly distort the lineshape.

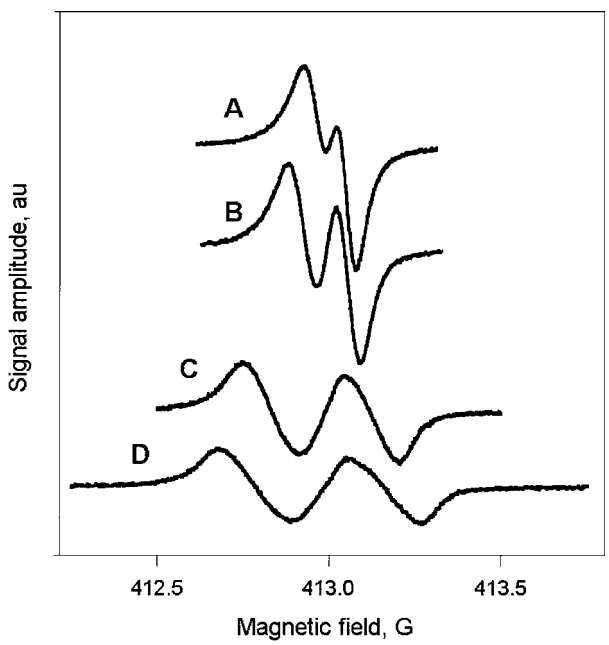

FIG. 4. EPR spectra of the LiPc phantom as a function of magnetic field gradient: The spectra in Figs. 4A–4D correspond to $gradB = 0.6$, 0.9, 2.1, and 2.7 G/cm, respectively. The low field line belongs to the LiPc crystal at 2% O_2 and the high field line to the crystal at 1% O_2.

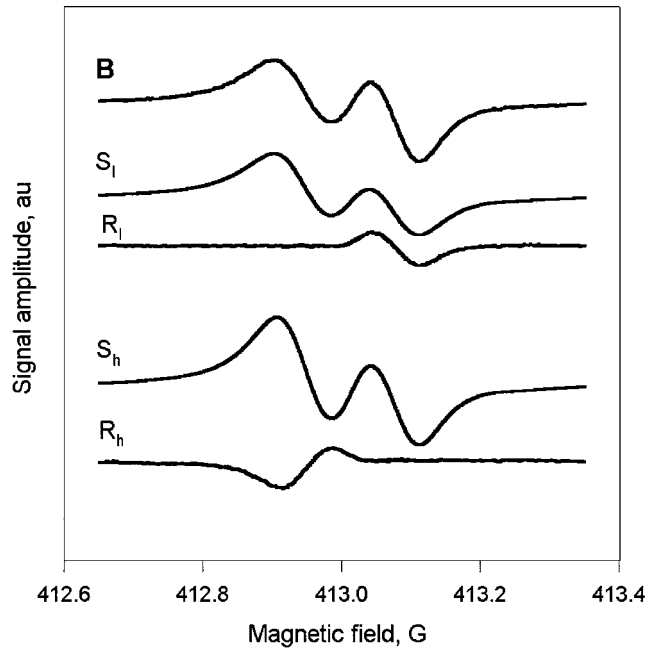

FIG. 5. Fitting of spectrum in Fig. 4B of the phantom using spectrum in Fig. 4C as an envelope function. S_l and S_h are the best-fit spectra obtained by choosing the low and high field intervals, respectively. R_l and R_h are the fit residuals (differences between the experimental and the simulated spectra) corresponding to the chosen field intervals.

Figure 5 shows the results of our convolution-based fitting method applied to the spectrum in Fig. 4B using that in Fig. 4C as an envelope function. Because the goal was to derive the undistorted EPR linewidth of LiPc in each individual capillary, the entire spectrum was divided into two intervals to be fit. Initially, a least-squares optimization was carried out first for the part of the spectrum that contained the low field line (2% O_2) and then for the part containing the high field line (1% O_2). The simulated spectra for the low and the high field lines, S_l and S_h respectively, and the corresponding residuals (differences between the experimental and the simulated spectra), R_l and R_h, are also shown in Fig. 5. For each of the sites the residuals demonstrate excellent fits within the corresponding intervals. Figure 6 summarizes the linewidths derived from the fitting of different spectral pairs. It appears that independent measurement of the linewidth using the combination of different spectral pairs could provide a trustworthy linewidth measurement. Also, processing a series of spectra (i.e., taking multiple measurements) could be used to improve the accuracy through data averaging.

Pilot In Vivo Experiments

A simple reliability test of the method was performed with a single LiPc implant in the cortex of the rat brain. In order to

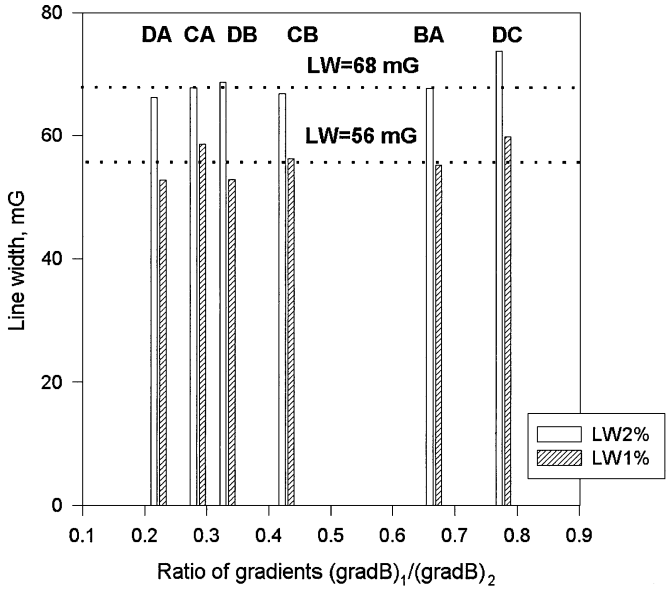

FIG. 6. The linewidths as a function of the gradients ratio $(gradB)_1/(gradB)_2$ for the phantom. The linewidths were derived from least-squares fitting of different combinations of the spectral pairs shown on top. The dotted lines show the actual EPR linewidths (56 and 68 mG) of LiPc in the capillaries.

exclude uncontrolled biological variations of the pO_2, the EPR spectra were taken sequentially in the following order: without a magnetic field gradient, with the gradient, and then again without the gradient. The linewidths measured from spectra recorded without the gradient are 209 ± 1 and 195 ± 1 mG. EPR spectra recorded with moderate field gradients showed some gradient-induced broadening: the peak-to-peak widths of the distorted spectra (shown in Figs. 7A and 7B) are 265 ± 2 mG ($gradB =$ 2.4 G/cm) and 222 ± 1 mG ($gradB = 1.2$ G/cm), respectively. In order to derive the undistorted linewidth from these data, the spectrum in Fig. 7A was rescaled (not shown) and used as an envelope function for fitting the spectrum in Fig. 7B (Eq. [6]).

From this fitting the undistorted linewidth of 200 ± 2 mG ($pO_2 = 33.3$ mm Hg accordingly) was obtained. This value is in good agreement with the linewidths measured without a gradient (209 ± 1 mG). Figure 7 also shows the simulated spectrum in Fig. 7C and the residual in Fig. 7D, which does not show any systematic deviation. Asymmetry in the simulated spectrum is caused by a dispersive contribution that was included as an adjustable parameter in the simulations.

Figure 8 illustrates simultaneous measurements of cerebral pO_2 in two hemispheres of the rat brain. EPR signals from two LiPc implants located 5 mm apart were separated by a magnetic field gradient: the spectrum in Fig. 8A recorded at a magnetic field gradient of 3.68 G/cm was used as an envelope function to fit the spectrum in Fig. 8B, which was recorded at a smaller gradient of 1.84 G/cm. Spectra in Figs. 8A and 8B are shown in a magnetic field scale as recorded. The results of the fitting are shown as two groups, I and II, consisting of two spectra each. Groups I and II illustrate the fitting of the low field feature (from the left hemisphere) and the high field feature (from the right hemisphere), respectively. The linewidths derived from the fitting procedure are 147 ± 6 and 93 ± 3 mG for the low and the high field lines, respectively (corresponding pO_2 are 23 ± 1 and 12 ± 0.5 mm Hg). Least-squares optimization was carried out separately for the low and high fields lines, and corresponding simulated spectra in Fig. 8 are labeled S_l and S_h. The residuals, R_l and R_h, do not show any systematic deviations between the experiment and the fit over the fitting intervals (Fig. 8).

By increasing the magnitude of the magnetic field gradient, one should be able to resolve the EPR lines that belong to individual LiPc crystals within a single implant. This is illustrated in Fig. 9, which shows the EPR spectra of a single LiPc implant in a RIF—1 mice tumor. The spectrum in Fig. 9A at the top was recorded with a magnetic field gradient of 1.69 G/cm. Figure 9B shows the spectrum of the same implant recorded at a larger gradient of 2.54 G/cm. At least three partially resolved lines are seen in these spectra. We used our method to fit the spectra within the intervals corresponding to each of the partially resolved lines and derived the undistorted linewidth of each of the spectral features. Three residuals, R_l, R_c, and R_h, illustrate that our model works well for low, central, and high field lines of

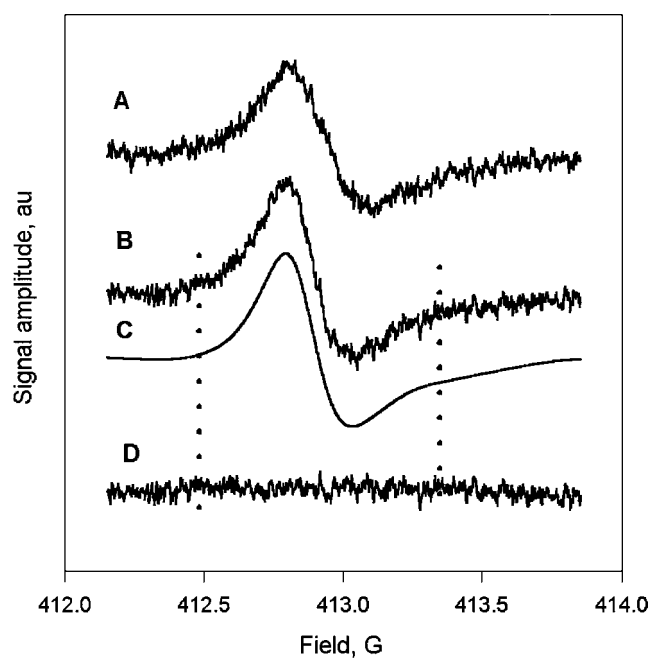

FIG. 7. A test of the fitting procedure using EPR spectra of a single LiPc implant in a rat brain. Spectra in Figs. 7A and 7B were recorded at gradients 2.4 and 1.2 G/cm, respectively. The interval between the dotted lines was used to fit the rescaled spectrum in Fig. 7A (envelope function) to the spectrum in Fig. 7B. The spectrum in Fig. 7C was calculated using the parameters of the fitting. The residual in Fig. 7D (the difference between the spectra in Figs. 7B and 7C) does not show any systematic deviations between the experiment and the fit over the fitting interval and is essentially a random noise.

the spectrum (the spectrum in Fig. 9B was used as an envelope). The results of the fittings give $pO_2 = 0.8 \pm 0.4$ mm Hg for the low, 8.8 ± 0.5 mm Hg for the high, and 17.3 ± 0.9 mm Hg for the central field portions of the EPR spectrum from the implant. Thus, in principle, our method could be used to measure pO_2 in three or more points simultaneously, and thus to characterize the spatial distribution of pO_2 in tumors and tissues.

Another example of the multi-site EPR oximetry fitting method of even higher spatial resolution is shown in Fig. 10. In the presence of large magnetic field gradients, two spectral features are clearly observed in the EPR spectra of the single LiPc implant in a rat brain (spectra in Figs. 10B and 10C). The maximum of the splitting between these two lines is observed in the direction perpendicular to the skull. They arise from two edges of the implant and report two very different pO_2 values. The crystals located closer to the skull indicated 7.5 ± 0.3 mm Hg, while the crystals located deeper in the cortex reported 22.3 ± 0.9 mm Hg. Using the splitting between these two lines and the gradient value, the size of the implant was evaluated as 0.36 mm along the direction of the magnetic field gradient. Reliability of these measurements was further confirmed by using the combination of different spectral pairs. Figure 11 illustrates that the pO_2 values derived from each spectral pair are consistent.

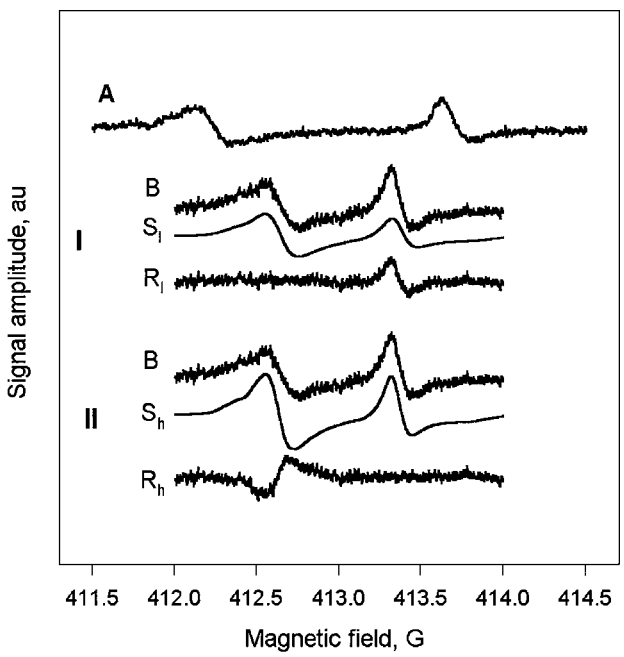

FIG. 8. Simultaneous measurements of the cerebral pO_2 in both hemispheres of a rat brain. Spectra in Figs. 8A and 8B were recorded at $gradB = 3.68$ and 1.84 G/cm, respectively. Two groups of three spectra each are labeled I and II and illustrate separate fitting of the low- and high-field portions of the same spectrum in Fig. 8B, using that in Fig. 8A as an envelope. S_l and S_h are the simulated spectra and R_l and R_h are the corresponding residuals for the low- and high-field lines, respectively.

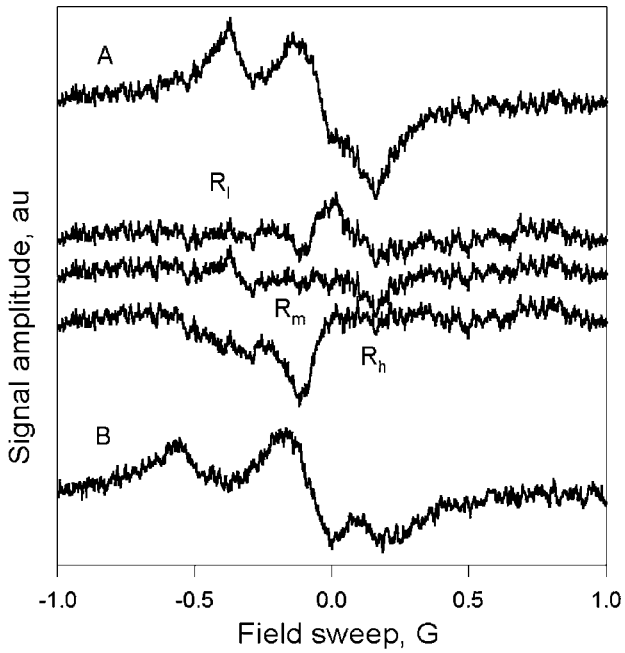

FIG. 9. Fitting of the spectrum in Fig. 9A from a single LiPc implant in RIF-1 mice tumor recorded in the presence of a magnetic field gradient $(gradB)_1 = 1.69$ G/cm (at the top of the figure) using the spectrum in Fig. 9B from the same implant (at the bottom of the figure) recorded at a larger field gradient $(gradB)_2 = 2.54$ G/cm, applied in the same direction. Three fitting intervals were used to fit partially resolved lines seen on this spectrum; R_l, R_c, and R_h are the residuals for the low-, central-, and high-field parts of the spectrum, respectively.

DISCUSSION

The results of model simulations and *in vivo* EPR experiments demonstrate that even when the EPR spectra from different sites are only partially resolved by one-dimensional magnetic field gradients, the individual spectral features could be examined separately and the corresponding undistorted Lorentzian linewidths can be determined using the digital procedures we described. Our method, based on the relationship between two EPR spectra $J_1(r)$ and $J_2(r)$ given by Eq. [6], is very convenient because it allows accurate and efficient determination of the width of the EPR spectrum $\Delta B_{1/2}$ (if the shape is Lorentzian) by least-squares fitting. During the Levenberg–Marquardt optimization, the width, double-integrated intensity, and position of the Lorentzian linewidth function $f(r, \Delta r_{1/2})$ can be adjusted so the result of digital convolution matches another experimental spectrum $J_1(r)$.

An alternative way to extract $\Delta r_{1/2}$ from Eq. [6] is to find the form of $f(r, \Delta r_{1/2})$ by carrying out deconvolution using, for example, Fourier-transform-based or iterative algorithms (*22–24*). However, the results of digital deconvolution are known to be very unstable to experimental noise, especially when the effective widths of the experimental spectra $J_1(r)$ and $J_2(r)$ exceed that of $f(r, \Delta r_{1/2})$. In a contrast to that, our

convolution-based fitting approach parameterizes the broadening function $f(r, \Delta r_{1/2})$ and this results in a significant reduction of the amount of calculations that need to be made and in improving of the accuracy of the fitting procedure. Also, because there is no filtering in our method, the width of $f(r, \Delta r_{1/2})$ remains undistorted, compared to the results of digital deconvolution. Another useful feature of the Levenberg–Marquardt optimization algorithm is that it provides an estimate of the uncertainties in the extracted parameters. Additionally the method can account for a phase shift in the microwave (i.e., different amount of dispersion signal) between the experimentally measured $J_1(r)$ and $J_2(r)$.

Our fitting model (Eq. [6]) was derived under an assumption that the lineshape is well modeled by a Lorentzian function. Therefore, the method also would be applicable for spectra that are modeled by several overlapping Lorentzian functions. In the latter case, the fitting should be carried out with not one, but with a sum of several Lorentzian broadening functions f. However, Eqs. [7] and [8] are still applicable for recovering the undistorted linewidths for the individual function. It is worth noting that our technique could be applied successfully if two major experimental conditions are fulfilled:

1. The key assumption is that only a limited number of particles of the probe material are present so the corresponding EPR lines can be resolved with a one-dimensional magnetic field gradient. If the sites are not resolved with the chosen gradient, then the direction and/or amplitude of the gradient should be varied for optimal resolution.

2. Another condition for the magnetic field gradient is that for a sample with a distribution of oxygen concentrations, the magnitude *grad*B should be much greater than that of the gradient of linewidth *grad*$(\Delta B_{1/2})$. In other words, within an interval of a spectrum with a width $\Delta B \gg \Delta B_{1/2}$ the EPR linewidth and oxygen concentration should be accepted as constants. One might say that this condition is easy to satisfy by applying magnetic field gradients of larger magnitudes. However, larger gradients decrease the signal intensity due to line broadening, and therefore the maximum magnitude of the gradient is restricted by EPR sensitivity.

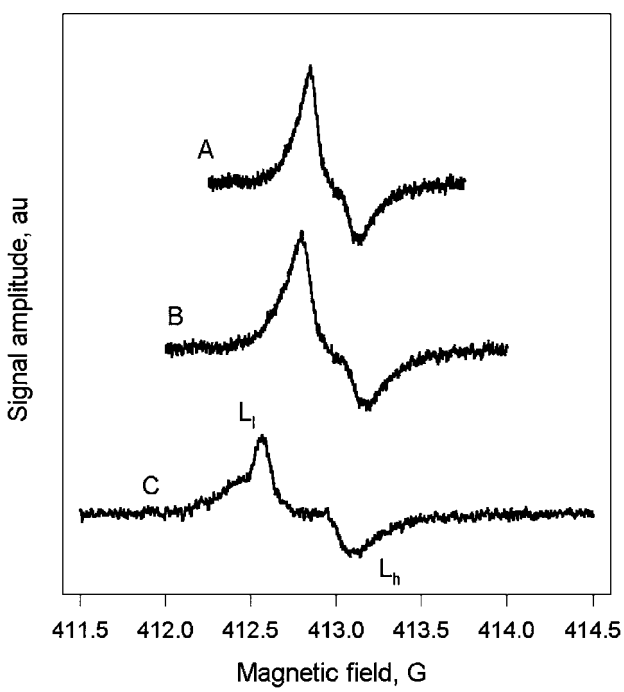

FIG. 10. EPR spectra of a LiPc implant in a rat brain as a function of magnetic field gradient. Spectra in Figs. 10A–10C were recorded at 3.69, 5.53, and 8.3 G/cm, respectively. L_l and L_h indicate low- and high-field spectral features arising from two edges of the implant. These features become clearly resolved in the presence of the largest field gradient (8.3 G/cm).

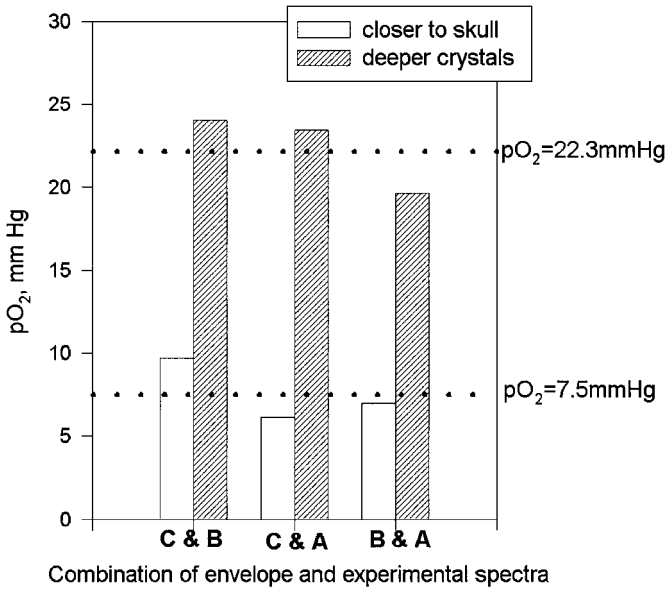

FIG. 11. The pO_2 values derived by combinations (shown at the bottom of the figure) of different spectral pairs from Fig. 13. The dotted lines show the mean pO_2 values, 7.5 and 22.3 mm Hg, at the edges of the implant.

CONCLUSIONS

We have demonstrated that the convolution-based fitting method extends the applications of multi-site EPR oximetry and improves the spatial resolution. The data acquisition time is increased marginally because only one additional spectrum is required, compared with the original method. To increase the accuracy, more scans could be taken and combinations of different spectral pairs could be used.

EXPERIMENTAL

LiPc crystals were synthesized at the Dartmouth EPR Center by a modification of previously described procedures (*25*). For the experiments we used needle-shaped 0.2–0.5-mm long

single crystals. At 37°C these crystals exhibit a single line EPR spectrum with $g \sim 2.002$ and a Lorentzian lineshape with the linewidth proportional to pO_2 ($\Delta B_{p-p} = 30$ mG in the absence of oxygen and $\Delta B_{p-p} = 812$ mG when equilibrated with atmospheric oxygen). The extremely narrow line (at anoxic conditions) and a high density of paramagnetic centers (up to 1×10^{20} spins/g), permit the use of even submillimeter size crystals for measurements with low frequency EPR.

All measurements were carried out with an L-band (1.2 GHz) EPR spectrometer utilizing a microwave bridge and an external loop resonator specially designed for experiments *in vivo* (*26*, *27*).

The feasibility of the method for *in vivo* measurements was demonstrated on pO_2 measurements carried out in a murine subcutaneous radiation-induced fibrosarcoma (RIF-1) tumor and in the cerebral cortex of the rat brain. The animals were C3H/HeJ mice and male Sprague–Dawley rats (18 and 290 g, respectively, Charles River Lab., MA). RIF-1 tumor cells were grown *in vitro* and implanted subcutaneously into the right hind leg of a mouse approximately 2 weeks before the EPR experiment. Several days before the experiments, LiPc crystals (about 50 μg) were implanted into the tumors in the mouse or in the cerebral cortex of the rat brain using 25-gauge needles with the animals under ketamine/xylazine anesthesia. The depth of injection was approximately 2 mm from the surface of the tumor or the skull.

For EPR oximetry measurements, an animal (under anesthesia) was placed between the poles of the electromagnet of the EPR spectrometer and the "external-loop" resonator was positioned just above the region where the implanted LiPc crystals were located. A set of coils capable of generating a magnetic field gradient in any direction with a magnitude up to 10.0 G/cm was used. The EPR spectra of LiPc were recorded under conditions that avoided microwave power saturation and distortions due to over-modulation. Typical scan time was 10 s. Least-squares fitting was carried out with the EWVoigt program (Scientific Software Services, Bloomington, IL).

The linewidth errors were estimated using a standard covariance matrix method as described in (*18*). These errors correspond to 68% confidence interval. All linewidths are reported as peak-to-peak.

ACKNOWLEDGMENTS

This work was supported by NCRR and NIH Grant, "EPR Center for the Study of Viable Systems," RR 11602 and NIH Grant Program Project GM 51630. A. I. S. is thankful to the North Carolina State University for support.

REFERENCES

1. H. M. Swartz, S. Boyer, and P. Gast, J. F. Glockner, H. Hu, K. J. Liu, M. Moussavi, S. W. Norby, T. Walczak, N. Vahidi, M. Wu, and R. B. Clarkson, Measurements of pertinent concentrations of oxygen in vivo, *Magn. Reson. Med.* **20,** 333–339 (1991).
2. J. F. Glockner and H. M. Swartz, In vivo EPR oximetry using two novel probes: Fusinite and lithium phthalocyanine, *in* "Oxygen Transport to Tissue XIV" (W. Erdmann and D. F. Bruley, Eds.), pp. 229–234, Plenum, New York (1992).
3. K. J. Liu, P. Gast, and M. Moussavi *et al.*, Lithium phthalocyanine: A probe for EPR oximetry in viable biological systems, *Proc. Natl. Acad. Sci.* **90,** 5438–5442 (1993).
4. N. Vahidi, R. B. Clarkson, K. J. Liu, S. W. Norby, M. Wu, and H. M. Swartz, In vivo and in vitro EPR oximetry with fusinite: A new coal-derived, particulate EPR probe, *Magn. Reson. Med.* **31,** 139–146 (1994).
5. K. J. Liu, G. Bacic, and P. J. Hoopes, J. Jiang, H. Du, L. Ou, J. F. Dunn, and H. M. Swartz, Assessment of cerebral pO_2 by EPR oximetry in rodents: Effects of anesthesia, ischemia, and breathing gas, *Brain Res.* **685,** 91–98 (1995).
6. P. James, O. Y. Grinberg, F. Goda, T. Panz, J. O'Hara, and H. M. Swartz, Gloxy: An oxygen-sensitive coal for accurate measurement of low oxygen tensions in biological systems, *Magn. Reson. Med.* **37,** 48–58 (1997).
7. J. A. O'Hara, P. E. James, T. Panz, O. Y. Grinberg, N. Jain, J. Dunn, and H. M. Swartz, Determining the anatomic position and histological effects in tumors of gloxy, an oxygen sensitive paramagnetic material, *Adv. Exp. Med. Biol.* **428,** 107–113 (1997).
8. H. M. Swartz and R. B. Clarkson, The measurement of oxygen in vivo using EPR techniques, *Phys. Med. Biol.* **43,** 1957–1975 (1998).
9. K. J. Liu, P. J. Hoopes, and E. L. Rolett, B. Beerle, A. Azzawi, F. Goda, J. F. Dunn, and H. M. Swartz, Effect of anesthesia on cerebral tissue oxygen and cardiopulmonary parameters in rats, *Adv. Exp. Med. Biol.* **428,** 33–39 (1997).
10. S. Taie, S. B. Leichtweis, K. J. Liu, M. Miyake, O. Y. Grinberg, E. Demidenko, and H. M. Swartz, The effects of ketamine/xylazine and pentobarbital anesthesia on cerebral tissue oxygen tension, blood pressure, and arterial blood gas in rats, *Adv. Exp. Med. Biol.* **471,** 189–198 (1999).
11. H. M. Swartz, S. Taie, M. Miyake, O. Y. Grinberg, H. Hou, H. El-Kadi, and J. F. Dunn, The effects of anesthesia on cerebral tissue oxygen tension: Use of EPR oximetry to make repeated measurements, *in* "Oxygen Transport to Tissue XXII" (J. F. Dunn and H. M. Swartz, Eds.), Pabst Science, Lengerich (in press).
12. O. Y. Grinberg, M. Miyake, H. Hou, R. P. Steffen, and H. M. Swartz, The dose-dependent effect of RSR13, a synthetic allosteric modifier of hemoglobin, on physiological parameters and brain tissue oxygenation in rats, *in* "Oxygen Transport to Tissue XXII" (J. F. Dunn and H. M. Swartz, Eds.), Pabst Science, Lengerich (in press).
13. M. Miyake, O. Y. Grinberg, H. Hou, R. P. Steffen, H. El-Kadi, and H. M. Swartz, The effect of RSR13, a synthetic allosteric modifier of hemoglobin, on brain tissue pO_2 (measured by EPR oximetry) following severe hemorrhagic shock in rats, *in* "Oxygen Transport to Tissue XXII" (Dunn, J. F. and H. M. Swartz eds.), Pabst Science, Lengerich (in press).
14. O. Y. Grinberg, H. Hou, and H. M. Swartz, Direct repeated measurements of pO_2 in the brain during ischemia and reperfusion, *in* "Ischemic Blood Flow in the Brain," Keio University Symposia for Life Science and Medicine (Y. Fukuuchi, M. Tomita, and A. Koto, Eds.), Vol. 6, pp. 381–389, Springer-Verlag, Tokyo (2000).
15. A. I. Smirnov, S. W. Norby, R. B. Clarkson, T. Walczak, and H. M. Swartz, Simultaneous multi-site EPR spectroscopy in vivo, *Magn. Reson. Med.* **30,** 213–220 (1993).
16. E. V. Galtseva and O. E. Yakimchenko, Spatial distribution reconstruction by EPR tomography in case of several magnetically nonequivalent centers, *VINITI*, No. 6180–6184, 26 (1984). [in Russian]
17. E. V. Galtseva, O. Y. Yakimchenko, and Y. S. Lebedev, Diffusion of free radicals as studied by tomography, *Chem. Phys. Lett.* **99,** No. 4, 301–304 (1983).
18. A. I. Smirnov, R. B. Clarkson, and R. L. Belford, EPR linewidth (T2) method to measure oxygen permeability of phospholipid bilayers and its use to study

the effect of low ethanol concentrations, *J. Magn. Reson. B* **111,** 149–157 (1996).

19. A. I. Smirnov and R. L. Belford, Rapid quantitation from inhomogeneously broadened EPR spectra by a fast convolution algorithm, *J. Magn. Reson. A* **98,** 65–73 (1995).

20. T. I. Smirnova, A. I. Smirnov, R. B. Clarkson, and R. L. Belford, Accuracy of oxygen measurements in T_2 (linewidth) EPR oximetry, *Magn. Reson. Med.* **33,** 801–810 (1995).

21. D. R. Duling, Simulation of multiple isotropic spin–trap EPR-spectra, *J. Magn. Reson. B* **104,** 105–110 (1994).

22. U. Ewert and K. U. Thiessenhusen, Deconvolution for stationary gradient method, *in* "EPR Imaging and In Vivo *EPR*" (G. R. Eaton, S. S. Eaton, and K. Ohno, Eds.), Chap. 11, pp. 119–126, CRC Press, Boca Raton (1991).

23. O. E. Yakimchenko, A. I. Smirnov, and Y. S. Lebedev, The spin probe technique in the EPR imaging of structurally heterogeneous media, *Appl. Magn. Reson.* **1,** No. 1, 1–19 (1990).

24. A. I. Smirnov, O. E. Yakimchenko, H. A. Golovina, S. K. Bekova, and Y. S. Lebedev, EPR imaging with natural spin probes, *J. Magn. Reson.* **91,** 386–391 (1991).

25. P. Turek, J. J. Andre, A. Giraudeau, and J. Simon, Preparation and study of a lithium phthalocyanine radical-optical and magnetic-properties. *Chem. Phys. Lett.* **134,** No. 5, 471–476 (1987).

26. M. Nilges, T. Walczak, and H. M. Swartz, 1 GHz in vivo EPR spectrometer operating with a surface probe, *Phys. Med.* **5,** 195–201 (1990).

27. H. Hirata, T. Walczak, and H. M. Swartz, Electronically tunable surface-coil-type resonator for *L*-band EPR spectroscopy, *J. Magn. Reson.* **142,** 159–167 (2000).